Mechanism underlying dynamic scaling properties observed in the contour of spreading epithelial monolayer

小熊，俊輝

Mechanism underlying dynamic scaling properties observed in the contour of spreading epithelial monolayer

Toshiki Oguma, Hisako Takigawa-Imamura ⦿, and Takashi Miura ⦿
Department of Anatomy and Cell Biology, Graduate School of Medical Sciences, Kyushu University, Japan

We found evidence of dynamic scaling in the spreading of Madin-Darby canine kidney (MDCK) cell monolayer, which can be characterized by the Hurst exponent $\alpha = 0.86$ and the growth exponent $\beta = 0.73$, and theoretically and experimentally clarified the mechanism that governs the contour shape dynamics. Dynamic scaling refers to the roughness of the surface scales, both spatially and temporally. During the spreading of the monolayer, it is known that so-called leader cells generate the driving force and lead the other cells. Our time-lapse observations of cell behavior showed that these leader cells appeared at the early stage of the spreading and formed the monolayer protrusion. Informed by these observations, we developed a simple mathematical model that included differences in cell motility, cell-cell adhesion, and random cell movement. The model reproduced the quantitative characteristics obtained from the experiment, such as the spreading speed, the distribution of the increment, and the dynamic scaling law. Analysis of the model equation shows that the model can reproduce different scaling laws from ($\alpha = 0.5$, $\beta = 0.25$) to ($\alpha = 0.9$, $\beta = 0.75$), where the exponents α and β are determined by two dimensionless quantities determined by the microscopic cell behavior. From the analytical result, parameter estimation from the experimental results was achieved. The monolayer on the collagen-coated dishes showed a different scaling law, $\alpha = 0.74$, $\beta = 0.68$, suggesting that cell motility increased ninefold. This result was consistent with the assay of the single-cell motility. Our study demonstrated that the dynamics of the contour of the monolayer were explained by the simple model, and we propose a mechanism that exhibits the dynamic scaling property.

I. INTRODUCTION

The shape of mammalian cell colonies varies, depending on the cell type and its environment. In the field of oncology, there is known to be a correlation between shape and malignancy of cancer, and suitable strategies for treatment can be inferred from analyzing the shape of cancer cell colonies [1]. To quantify the shape of these colonies, fractal analysis is often used. It has been reported that a high fractal dimension $\mathcal{D}$ reflects a heterogeneous contour shape, and that fractal dimension and cancer malignancy are likewise correlated [2]. Cancer cells show higher proliferation rates, higher motilities, and weaker cell-cell adhesion than benign cells [1]. These differences are thought to affect collective cell behavior and contribute to the roughness of contour shapes in cancer.

Cell movements are promoted by chemical or physical cues such as signal molecules and mechanical forces, in response to which cells modulate their downstream cytoskeleton by altering the subcellular localization of small G proteins such as RhoA, Rac1, and Cdc42 [3–5]. In collective cell migration, highly motile cells are often observed at the edge of the epithelial monolayer *in vitro*. Known as leader cells, these are characterized by having high Rac1 activity, thick actin filaments, and large cell bodies with spreading lamellipodia [6,7]. Leader cells can generate a driving force to spread the epithelial tissue and are often observed at the tips of monolayer protrusions [8–10]. However, the relationship between leader cells and the overall contour shape remains controversial. Mark *et al.* suggested that sharp curvature

promoted the appearance of the leader cells [11]. On the other hand, several studies have suggested that leader cells are determined by different mechanisms, such as mechanical force [12,13] and the Dll4-Notch1 pathway [14], and then form monolayer protrusions.

It is known that many curves in nature, such as the earth's surface in cross section and the interface of clouds, form self-affine fractal structures [15]. The self-affine fractal structures do not show self-similarity, such as Koch's curve and the Menger sponge. However, a similar curve can be obtained through statistical rescaling that involves changing the horizontal coordinates by a, while the vertical coordinates are changed by b, and $a = b^\alpha$ holds. The exponent α is called the Hurst exponent, and self-affine fractal structure is characterized by the Hurst exponent. The fractal dimension $\mathcal{D}$ is also used to quantify the roughness of the structure. It can be measured using the box-counting method [16,17]. It is known that α and the fractal dimension $\mathcal{D}$ satisfy $\alpha + \mathcal{D} = 2$ for a curve in two-dimensional space [16,18]. The simplest example of self-affine fractal structure is a Brownian curve, which is the trajectory of a particle undergoing Brownian motion plotted over time. Its fractal dimension is $\mathcal{D} = 1.5$ and its Hurst exponent is $\alpha = 0.5$.

For a growing interface, the local roughness $w(l, t)$ is defined as the standard deviation of the height of the interface, within a closed range of length l:

$$w(l, t) = \langle \sqrt{\langle [h(x, t) - \langle h \rangle_l]^2 \rangle_l} \rangle, \qquad (1)$$

where $\langle \cdots \rangle_l$ denotes the average value in the closed range. The quantity $h(x, t)$ is the "height" of the interface at the location x, and it represents the shape of the contour. Such a system is said to exhibit dynamic scaling when the following relationships are satisfied [17,19]:

$$w(l, t) \sim \begin{cases} l^\alpha & \text{for } l \ll l_*, \\ t^\beta & \text{for } l \gg l_* \end{cases}, \qquad (2)$$

where the length l_* increases as time evolves. The former equation confirms that the interface forms a self-affine fractal structure, and the latter means that the heterogeneity of the entire interface is scaled by the time. The exponent α is the Hurst exponent of the interface, and β is called the growth exponent.

Dynamic scaling has been identified in various phenomena, including bacterial colonies on agar [20,21], propagating slow combustion of paper [22], and growing interfaces in a turbulent liquid crystal [23]. In collective migration of vertebrate cells, the contours of cell colonies of HeLa and Vero cell lines were also found to exhibit dynamic scaling, with $\alpha = 0.50$ and $\beta = 0.32$ [24,25]. Some partial differential equations that show the properties of dynamic scaling are well known, including the Edwards-Wilkinson (EW) equation, the Kardar-Parisi-Zhang (KPZ) equation, and the Kuramoto-Sivashinsky (KS) equation. The EW equation is a stochastic partial differential equation with diffusion and spatiotemporally independent noise terms [26], the KPZ equation is similar to the EW equation but includes a nonlinear term [27], and the KS equation is a partial differential equation with the diffusion, nonlinear, and spatially fourth derivative terms [28]. Intriguingly, both the KPZ and KS equations are known to have the same Hurst and growth exponents, $\alpha = 1/2$ and $\beta = 1/3$. The sharing of similar scaling exponents between different phenomena and solutions is a property known as universality. In particular, the universality characterized by $\alpha = 1/2$ and $\beta = 1/3$ is called KPZ universality [27,29].

While various experimental systems that show dynamic scaling have been reported, to our knowledge, the underlying mechanisms that generate dynamic scaling laws are rarely considered [21]. In the current study, we aimed to uncover the mechanisms that lead to dynamic scaling properties in the contour of the epithelial monolayer, through experimental observations, numerical simulation, and analysis. In experiments, we observed the spreading of the Madin-Darby canine kidney (MDCK) cell monolayer and found that its time evolution followed a dynamic scaling law that was distinct from the KPZ universality. Our observations and mathematical model showed that the proportion of leader cells and cell-cell adhesion both play critical roles in the dynamics of the contour. From analytical consideration, we find that α and β are determined by the intensity of the random movement relative to differences of cell motility.

II. MATERIALS AND METHODS

A. MDCK cell culture

MDCK II cells were cultured using Eagle's minimal essential medium (MEM; Nacalai tesque) containing 10% fetal bovine serum (FBS) and 100 U/ml penicillin-streptomycin (Nacalai tesque), and maintained in a 5% CO_2 controlled atmosphere at 37 °C.

B. Fabrication of PDMS sheets

Polydimethylsiloxane (PDMS) sheets, used to create a cell-free regions, were prepared in the following manner: A well-mixed PDMS (Sylgard 184, Toray) precursor solution, with a 10:1 ratio of prepolymer to curing agent, was poured onto a flat polystyrene plate to a thickness of 1 mm and then cured in a drying oven at 80 °C for 2 h. After curing, 8-mm PDMS disks with 3- or 4-mm holes were created using biopsy punches (Maruho).

C. Cell patterning

The PDMS sheets were placed on the surface of a 27-mm glass-bottom dish (IWAKI), and the holes in the sheets were filled with MEM (without air bubbles), along with 2 ml of MDCK cells suspended in medium (2.5×10^5 cells/ml). Samples were incubated at 37 °C and 5% CO_2 for 48–72 h, until cells reached confluence within the holes of the sheets, and then the PDMS sheets were gently removed and samples were washed with MEM twice. The medium was changed with fresh medium containing CellTracker green CMFDA (5-chloromethylfluorescein diacetate) dye (5 μM; Invitrogen) and Hoechst33342 (1 μg/ml; Dojindo). After 4 h of incubation, the time-lapse observation was performed. The collagen-coated dishes were prepared with 27-mm glass-bottom dishes and type I-c collagen solutions (100 μg/ml; Nitta Gelatine).

D. Time-lapse microscopy

The time-lapse observations were performed using a Nikon A1 confocal microscope with a 10× or 20× objective lens. The cells were maintained in a 5% CO_2 controlled atmosphere at 37 °C. Images were acquired every 20 min (for Fig. 3) or 30 min (for Figs. 2, 6, and S5 [30]) until 18 h had elapsed after the PDMS sheet removal.

E. Measurement and quantification of cell spreading

The fluorescence microscopy images were numerically converted and analyzed quantitatively using IMAGEJ (National Institute of Health), PYTHON, and MATHEMATICA (Wolfram). The images were binarized to capture the shape of the monolayer, with the threshold values for binarization determined and set manually. We defined the centroid as the center of gravity of the cell monolayer in the initial image. The distance $D(\theta)$ from the centroid to the contour was measured along 2000 directions, with constant intervals. The mean front distance was calculated as $\langle D(\theta) \rangle(t) = \sum_\theta D(\theta)/2000$. The Hurst exponents were calculated as the slopes of the fitted lines in the log-log plot of $w(l, t)$ and l within the range of $l \in [2\Delta x, 10\Delta x]$. Here, Δx was defined by $2\pi \langle D(\theta) \rangle /2000$. The growth exponents were calculated as the slope of the fitted lines in the log-log plot of $w(l_{\max}, t)$ and t. The values shown in Figs. 2(b), 2(c), 2(e), 6(a), and S5(c) [30] are averages of the experimentally obtained values.

The rate of expansion in our observation may be relatively small compared to previous studies of fractal analysis

[21,23,24]. Whether or not the expansion is sufficient to explore the self-affine fractal and scaling property can be evaluated from the range of heterogeneity of the contour. At $t = 18$ h, the value of $w(l, t)$ reached about 80 μm (Fig. 2), which is almost the same order of magnitude as the heterogeneity reported by Huergo *et al.* [24]. Therefore, we consider that the contour is sufficiently heterogeneous and that it is reasonable to discuss the scaling law.

F. Cell tracking

We labeled cell nuclei with Hoechst33342, and images were obtained from 1 to 18 h after PDMS removal and analyzed with IMAGEJ, using the TrackMate plugin [31] to manually track the centers of cell nuclei. We considered cells whose nuclei were located within 30 μm of the contour to be at the edge of the monolayer. The contours were determined from the bright-field images and manually traced with segmented lines.

G. Cell staining

MDCK cells were washed with phosphate-buffered saline (PBS), fixed with 4% paraformaldehyde for 10 min, and permeabilized in 0.1% Triton X-100/PBS for 10 min. After washing, cells were stained with Alexa Fluor 555 Phalloidin (1:40; Invitrogen) and Hoechst33342 (1:2000; Dojindo). Cells were incubated for 30 min at room temperature before observation. Fluorescent and phase-contrast images were acquired using a BZ-X810 fluorescence microscope (Keyence) with $20\times$ objective lens.

H. Numerical simulation

The numerical simulations were performed using MATHE-MATICA and JULIA, and we used the explicit Euler scheme for calculating the time evolution.

I. Single-cell tracking assay

MDCK cells were seeded onto the 27-mm glass-bottom dish (2.5×10^4 cells/ml). The cells were incubated at 37 °C and 5% CO_2 for 24 h until the cells adhered to the bottom of the dish. Hoechst33342 (1:2000) was added to the dish and incubated for 30 min. Images were acquired using a Nikon A1 confocal microscope at 5-min intervals over a span of 2 h. The centers of cell nuclei were manually tracked using the TrackMate plugin, and statistical analysis was performed in MATHEMATICA, using Student's t-tests to compare experimental groups.

III. RESULTS

A. Epithelial monolayer spreading

To investigate how the epithelial monolayer spread, MDCK cells were cultured in the closed circular area confined within the PDMS sheet. Time-lapse observations were performed after the removal of the PDMS sheet boundary (Fig. 1(a), Movie 1 in the Supplemental Material [30]).

While the contour of the epithelial monolayer was initially smooth and round, our observations revealed that it became
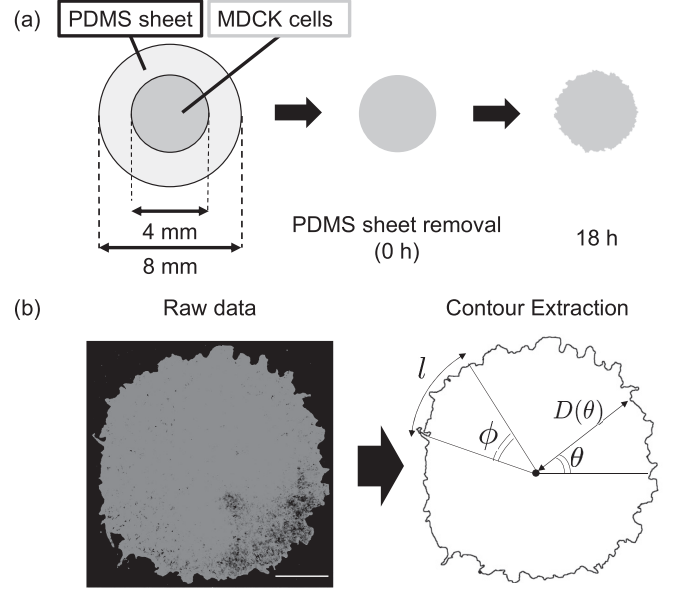

FIG. 1. Overview of the experimental method and measurement procedures. (a) Observation of MDCK migration. MDCK cells were seeded in the region confined by the PDMS sheet. After cells reached confluence, the PDMS sheet was removed and time-lapse observations were performed. (b) Measurement of the contour shape. The MDCK monolayer was visualized by CellTracker green, and the microscopy images were transformed into binarized images. The distances $D(\theta)$ from the center to the edge of the monolayer were measured. The orientation of the points along the contour was defined as θ ($0 < \theta < 2\pi$). The angle $\phi = l/\langle D \rangle(t)$ was defined from the unit of measurement l. Scale bar = 1000 μm.

rougher and more uneven over time, as cells migrated to the cell-free area. The epithelial cells kept contact with each other (Movie 1 in the Supplemental Material [30]). To quantify this, we measured the distance from the center to the edge of the monolayer, $D(\theta)$, where θ indicates the orientation of measurement points along the contour ($0 < \theta < 2\pi$) [Fig. 1(b)]. We chose 2000 points for measuring $D(\theta)$, to accurately reproduce the contour boundary during migration. The initial circumference (after the PDMS removal) was 1.26×10^4 μm. We found that the average $\langle D(\theta) \rangle$ increased linearly, at a rate of 11.2 μm/h, and the standard deviation of $D(\theta)$ also increased [Figs. 2(b) and 2(c)]. These results suggested that the epithelial monolayer spread at a constant speed with increasing heterogeneity of the contour.

We characterized the local roughness $w(l, t)$ of the circular geometry as follows:

$$w(l, t) = \langle \sqrt{\langle [D(\theta, t) - \langle D \rangle_\phi]^2 \rangle_\phi} \rangle \quad \phi = \frac{l}{\langle D \rangle}, \quad (3)$$

where t (h) is the time after PDMS removal and $\langle \cdots \rangle_\phi$ denotes the average value in the area ϕ. The local roughness $w(l, t)$ is the standard deviation of the distance $D(\theta)$ in the range of ϕ.

To examine whether the power law in (2) holds for the cell spreading, log-log plots were used to assess the relationship between local roughness $w(l, t)$ and l at different time points [Fig. 2(d)]. Within the range of small l, $\ln w(l, t)$ linearly increased along with increasing $\ln l$, indicating that
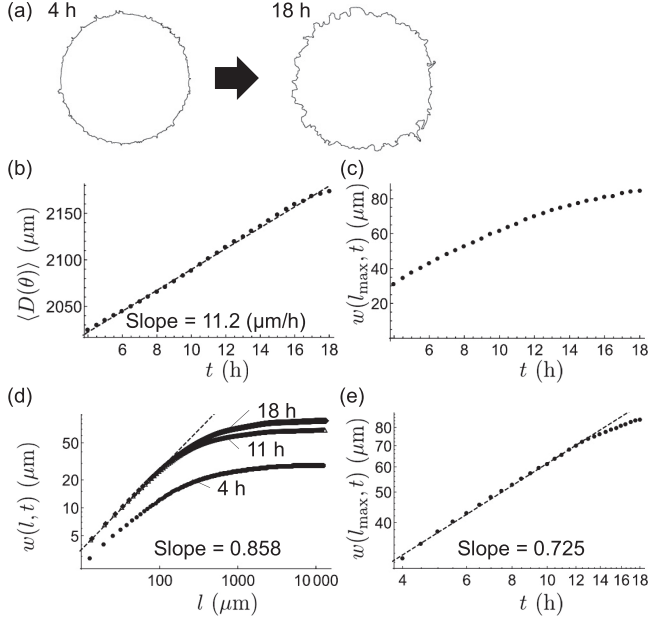
FIG. 2. Dynamic scaling law in the spreading of MDCK monolayer, obtained from experimental observations. (a) Contour of the MDCK monolayer, as it evolved from the initial smooth shape to the rough shape. (b) Time evolution of the average values of $D(\theta)$. Dots indicate the measured values, with the fitted line shown as dashed ($n = 6$). (c) Time evolution of $w(l_{\max}, t)$, the standard deviation of $D(\theta)$ ($n = 6$). (d) Measurement of the Hurst exponent. The plot shows the experimental results at different time points, and the black dashed line is the fitted line for $2\Delta x \leqslant l \leqslant 10\Delta x$ (μm) at 18 h. From this, the Hurst exponent was calculated as $\alpha = 0.858$. (e) Log-log plot of $w(l_{\max}, t)$ and t. Dots represent the measured values, and the black dashed line is the fitted line ($n = 6$). The growth exponent was calculated as $\beta = 0.725$.

the power law $w(l, t) \sim l^\alpha$ holds, which suggests the contour of the epithelial monolayer is a self-affine fractal structure. We also found the range of l that showed a linear relationship to expand over time, which is consistent with the well-known observation that l_* increases with time under the dynamic scaling law [17,29]. We determined the Hurst exponent to be $\alpha = 0.858$ for $t = 18$. For large l, the value of $w(l, t)$ approaches $w(l_{\max}, t)$, where $l_{\max} = 2\pi\langle D\rangle$. As shown in Fig. 2(e), $\ln w(l_{\max}, t)$ and $\ln t$ show a linear relationship, indicating that the power law $w \sim t^\beta$ holds. The growth exponent was $\beta = 0.725$. Thus, our observations revealed that the time development of the MDCK monolayer contour satisfied the dynamic scaling law. We repeatedly measured the exponents in different monolayers, and obtained values of $\alpha = 0.859 \pm 0.012$ and $\beta = 0.728 \pm 0.061$, which were not much different from the data shown in Fig. 2.

B. Cell behavior at the edge

To understand the dynamics of the evolving contour shape as the monolayer spreads, we observed and quantified the behavior of cells near the monolayer edge. Cell nuclei were visualized and tracked from $t = 1$ to $t = 18$ (Fig. 3(a), Movie 2 in the Supplemental Material [30]). Among cells initially

located in the edge region, 58% of these remained near the edge during the entire observation time, while 42% migrated toward the monolayer center. These internalizations were observed to result from the merging of monolayer protrusions. The decrease in the number of cells around the edge was compensated for by proliferation and the intercalation of internal cells. We reversely tracked cells near the edge at $t = 18$ and found that 77% of these were also near the edge at $t = 1$. In addition, the kymograph of the edge cell migration showed that movement toward the initially cell-free region first started among edge cells and then the inner cells followed (Fig. S1 [30]). These results suggested that the dynamics of the contour shape were primarily driven by the movements of cells at or near the edge.

Since leader cells are known to play an important role in the formation of monolayer protrusion, we next focused on their behavior and dynamics. Leader cells are characterized by their large lamellipodia, large cell bodies, and high motility. Cells with these characteristic shapes were observed as early as $t = 2$ [Fig. 3(b)]. As shown in Fig. 3(c) and Movie 3 in the Supplemental Material [30], we performed reverse tracking of the leader cells from $t = 18$ to $t = 1$. Leader cells were clearly distinguished by their locations and large cell bodies at $t = 18$. They were consistently at the edge throughout the observation period, formed the monolayer protrusions, stayed located at the tip, and had higher velocities than other cells (Fig. S2 [30]). The fact that leader cells remained located at the tip of the protrusion reflected their spontaneous high motility and suggested that the high motilities of the leader cells were maintained throughout the observation period. These results indicate that leader cells emerged at an early stage of the migration at the edge, and that their properties did not change.

C. Mathematical model and numerical simulation

Informed by the experimental results, we modeled the dynamics of the contour of the MDCK monolayer. We assumed that the contour dynamics arise from the movements of cells at the edge, and these cells have different motility. The model also assumes, based on a known property of epithelial cells, that cells interact through intercellular adhesion [Fig. 4(a)]. We described the dynamics of cells at the edge by means of temporally continuous and spatially discrete differential equations as follows:

$$\frac{d}{dt}\mathbf{r}_i(t) = \mathbf{M}_i + (\mathbf{T}_i - \mathbf{T}_{i+1}) + \sigma\eta_i(t)\mathbf{r}_i/|\mathbf{r}_i|, \quad (4)$$

where $\mathbf{r}_i(t)$ represents the coordinates of the cell i at time t, $\mathbf{M}_i$ is active, directional movement, and $\mathbf{T}_i$ describes passive movement due to the elastic force from cell-cell adhesion. The third term on the right-hand side represents random movement, with the constant σ indicating the intensity of noise, while $\eta_i(t)$ is spatially and temporally independent Gaussian white noise. At the cellular scale, the inertia force may be ignored.

The directional motility term $\mathbf{M}_i$ was given by

$$\mathbf{M}_i = \begin{bmatrix} v_l \, \mathbf{r}_i/|\mathbf{r}_i| & \text{(if the cell i is a leader cell)} \\ v_f \, \mathbf{r}_i/|\mathbf{r}_i| & \text{(otherwise)}, \end{bmatrix} \quad (5)$$
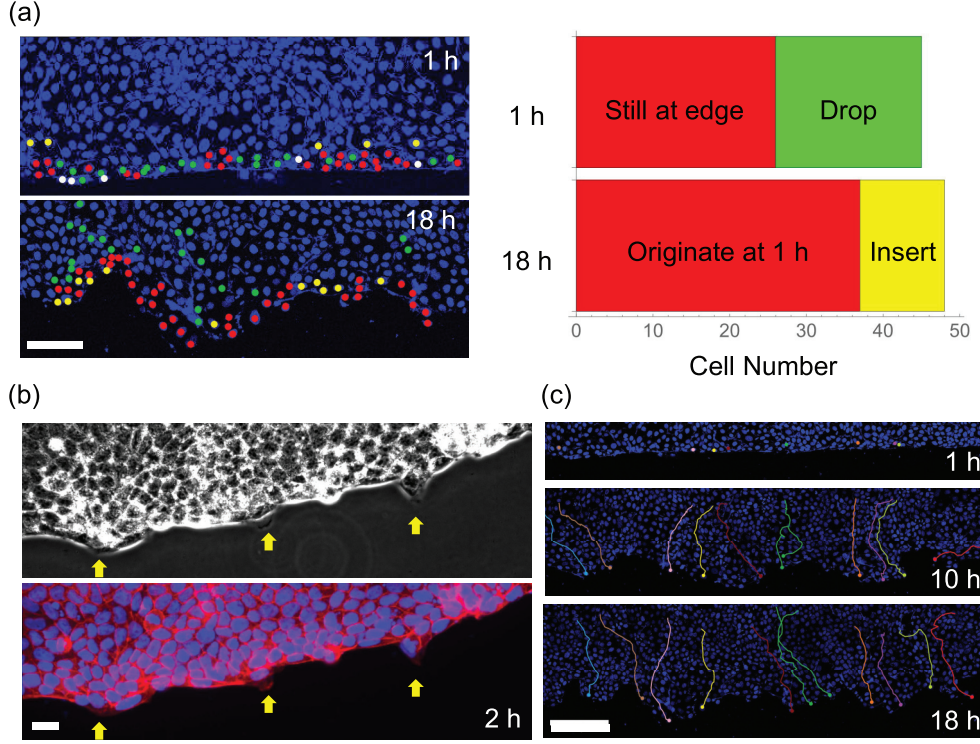
FIG. 3. Behavior of the cells at the edge of the monolayer. (a) Cell tracking at the monolayer edge. Nuclei were visualized with Hoechst33342 (left panels, blue signals). Cells that remained near the edge from $t = 1$ to $t = 18$ are indicated by red circles. Those cells that dropped and intercalated from the edge by $t = 18$ are indicated by green and yellow circles, respectively. Among 45 cells initially located at the edge, 19 cells dropped, while 11 cells divided (right panel). Those 11 cells newly intercalated to the edge, and therefore 77% of the edge cells at $t = 18$ are originated from the cells at the edge at $t = 1$. Scale bar = 100 μm. (b) Snapshot of the edge at $t = 2$. Large cells that stretch their lamellipodia were observed (indicated with yellow arrows). The upper panel is a phase-contrast image, and the lower panel is a fluorescent image; the nuclei and F-actin are represented in blue and red, respectively. Scale bar = 20 μm. (c) Behavior of leader cells during collective cell migration. Circles indicate leader cells, which were distinguished by their locations and large sizes. Lines in the middle panel show the trajectory of the cells from $t = 1$ to $t = 10$ and in the bottom panel show that from $t = 10$ to $t = 18$. Scale bar = 200 μm.

where v_l and v_f are the velocities of the leader and follower cells, respectively ($v_l > v_f > 0$). The ratio of leader cells to all edge cells is p_l, and the distribution of leader cells was randomly determined.

Assuming that intercellular interaction $\mathbf{T}_i$ linearly increases with the intercellular distance, $\mathbf{T}_i$ was given by

$$\mathbf{T}_i = \rho(\mathbf{r}_i - \mathbf{r}_{i-1}), \tag{6}$$

where ρ is the stiffness of elastic interaction.

We set the initial shape of the monolayer as a circle with a radius of 2000 μm. The total number of cells at the edge was set to $N = 2000$, aligned with a regular interval. For simplicity, the cell number change and rearrangement at the edge were omitted. The numerical results are shown in Fig. 4 and Movie 4 in the Supplemental Material [30]. The parameter p_l was estimated from the actual distribution of cells displaying large lamellipodia [Fig. 3(b)], and v_l and v_f were set such that the growth speed of the average diameter was consistent with the values obtained experimentally.

We found that the model (4) described and captured the process of cell sheet expansion well, as it was able to reproduce many of the properties observed in our experiments, as shown in Figs. 4(b) to 4(e). The time evolution of $\langle D(\theta) \rangle$ was linear, with a slope of 11.2 μm/h. The values of $w(l_{\max}, t)$ shown in Fig. 4(c) were similar to those in Fig. 2(c). The log-log plot of $w(l, t)$ against l showed a linear relationship for small l [Fig. 4(d)], and the Hurst exponent was calculated as $\alpha = 0.849$. The log-log plot of $w(l_{\max}, t)$ against t also showed a linear relationship [Fig. 4(e)], and the growth exponent was calculated as $\beta = 0.729$. In addition, the time evolution of $\text{Max}[D(\theta)]$, $\text{Min}[D(\theta)]$, and the distribution of the increment for θ were also similar to the experimental results (Fig. S3 [30]). Taken together, these results show that the model (4) explained the dynamic scaling law seen in the contour of the MDCK monolayer.

D. Analysis of mathematical model

In this section, we show that the Hurst and growth exponents were analytically estimated, then evaluate the effects of the cell-cell adhesion, the difference in cell motility, and the noise intensity in this system.

Assuming that N is sufficiently large, it can be regarded that the elastic force affects only the radial direction, thus the model was simplified to a one-dimensional flat model with
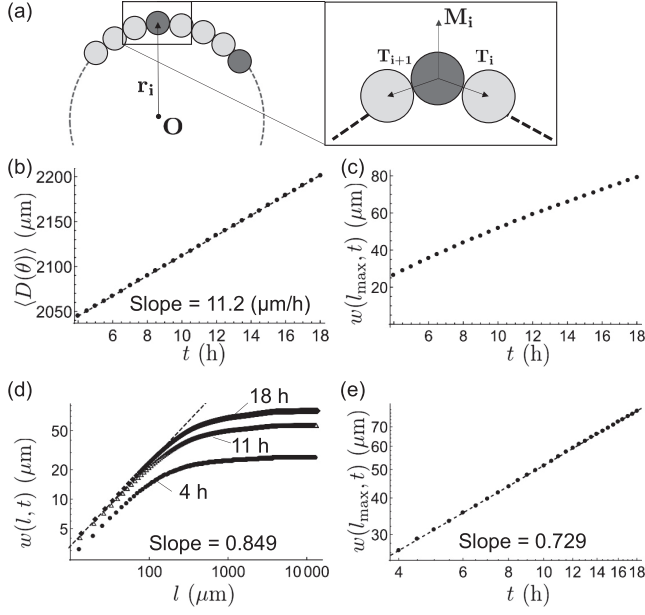
FIG. 4. Numerical simulation of the monolayer spreading. (a) Diagram of the mathematical model. Circles represent the cells at the edge, with the dark circles representing leader cells, and the light circles follower cells. The coordinates of the cell center are denoted by $\mathbf{r}_i$. Cells at the edge have different types of motility $\mathbf{M}_i$, and interact with neighboring cells through cell-cell adhesion $\mathbf{T}_i$. [(b)–(e)] Results from the numerical model corresponding to Figs. 2(b) to 2(e). (b) Time evolution of the average of the distance $D(\theta)$. (c) Time evolution of the standard deviation of $D(\theta)$ (global roughness). (d) Log-log plot of the local roughness $w(l, t)$ against l. (e) Log-log plot of the global roughness $w(l_{\max}, t)$ against t. Parameters: $v_l = 94$ [μm h^{-1}], $v_f = 2$ [μm h^{-1}], $p_l = 0.1$, $\rho = 6.67$ [h^{-1}], and $\sigma = 3$ [μm h$^{-1/2}$].

periodic boundary as follows:

$$\frac{d}{dt}h_x(t) = f_x + \rho(h_{x+1}(t) + h_{x-1}(t) - 2h_x(t)) + \sigma\eta_x(t).$$
(7)

Here $h_x(t)$ is the distance from the center to the cell x [for simplicity, set $h_x(0) = 0$], and f_x is the motility of the cell x that takes v_l or v_f. In probability p_l, the cell takes the higher motility $f_x = v_l$. The numerical calculation of the flat model (7) reproduced the characteristic dynamics with the dynamic scaling law generated by the circular model (4) (Fig. S4 [30]).

The exponents in the model (7) take different values depending on the parameters. When $v_l = v_f$, the model (7) is essentially the EW model, which includes the Gaussian white noise and the diffusion term. It is known that the EW model shows dynamic scaling $\alpha = 0.50$ and $\beta = 0.25$ [17,26]. On the other hand, if $\sigma = 0$, we call model (7) a "fixed-noise" model, and it shows dynamic scaling with $\alpha = 0.9$ and $\beta = 0.75$. This model exhibits dynamics driven by diffusion and the fixed noise, which arise from the spatial heterogeneity of the motilities.

Considering the discrete Fourier expansions of $h_x(t)$, f_x, and $\eta_x(t)$, the Fourier coefficients are denoted by $\hat{h}_k(t)$, $\hat{f}_k$, and $\hat{\eta}_k(t)$, respectively. The random variable $\hat{f}_k$ follows Gaussian

distribution denoted as $(v_l - v_f)\sqrt{p_l(1-p_l)}\hat{\mathcal{N}}(0, 1)$ (see the Supplemental Material A [30]). The complex Gaussian white noise $\hat{\eta}_k(t)$ satisfies $\int_s^t \hat{\eta}_k(t')dt' = \hat{\mathcal{N}}(0, t-s)$, where $\hat{\mathcal{N}}(0, 1)$ is a complex random variable that follows $\mathcal{N}(0, \frac{1}{2}) + i\mathcal{N}(0, \frac{1}{2})$ (see the Supplemental Material B [30]). We then obtained the differential equation for $\hat{h}_k(t)$ with $k \geqslant 1$ from (7) as follows:

$$\frac{d}{dt}\hat{h}_k(t) = \hat{f}_k - \left(4\rho\sin^2\frac{\pi k}{N}\right)\hat{h}_k(t) + \sigma\hat{\eta}_k(t).$$
(8)

$\hat{h}_k(t)$ was explicitly derived using the Ito integral as follows (see the Supplemental Material C [30]):

$$\hat{h}_k(t) = \frac{\hat{f}_k}{a_k}(1 - e^{-a_k t}) - \sigma\int_0^t e^{a(s-t)}d\hat{B}_s.$$
(9)

$\hat{B}_s$ is Brownian motion in the complex plane, and $a_k = 4\rho\sin^2\frac{\pi k}{N}$. Equation (9) indicates that the Fourier coefficient $\hat{h}_k(t)$ follows the complex Gaussian distribution with the mean $\frac{\hat{f}_k}{a_k}(1 - e^{a_k t})$ and the variance $\frac{\sigma^2}{2a_k}(1 - e^{-2a_k t})$. The expected value for the power spectrum $|\hat{h}_k(t)|^2$ is given by

$$E[|\hat{h}_k(t)|^2] = \frac{|\hat{f}_k|^2}{a_k^2}(1 - 2e^{-a_k t} + e^{-2a_k t}) + \frac{\sigma^2}{2a_k}(1 - e^{-2a_k t}).$$
(10)

Next, we introduce the squared local roughness $w^2(l, t)$ as the average of the variance of h_x in m consecutive cells. Using the intercell distance Δx and non-negative integer m, $w^2(l, t)$ is expressed as

$$w^2(l, t) = w^2(m\Delta x, t)$$
$$= R(0) - \frac{1}{m(m-1)}\sum_{l=1}^{m-1}2(m-l)R(l). \quad (11)$$

$R(l)$ is an autocorrelation function of h_x. Since $R(l)$ is obtained by inverse Fourier transform of the power spectrum $|\hat{h}_k(t)|^2$ (Winner-Khinchin's theorem), we obtained the expected value of $w^2(l, t)$ as in (11). Figure 5(a) shows that the analytically derived $w^2(l, t)$ was close to the average of the numerical calculations of the circular model.

Considering the slope of the log-log plots in Fig. 5(a), we derived the Hurst and growth exponents as follows:

$$\alpha = \ln\left[1 + \frac{1}{3}\frac{R(1) - R(2)}{R(0) - R(1)}\right]\Big/2\ln\frac{3}{2}, \quad (12)$$

$$\beta = \frac{t}{2w^2(l_{\max}, t)}\frac{\partial}{\partial t}w^2(l_{\max}, t). \quad (13)$$

We calculated the expected values $\alpha = 0.80$ and $\beta = 0.74$ for the parameters used for the circular model in Fig. 4. This confirmed that our analysis based on (7) captured the dynamics of the circular model in (4).

Equation (12) also shows that the Hurst exponent is represented as the ratio of the linear sum of the power spectra. Therefore, multiplying the power spectrum by a constant value should not affect the Hurst exponents. By dividing the power spectra (10) by σ^2/ρ, we found that the Hurst expo-
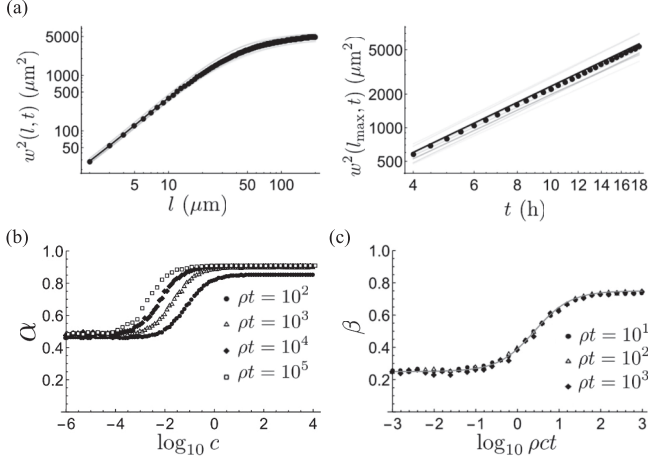
FIG. 5. Parameter dependency of the Hurst and growth exponents. (a) Comparison of numerically and analytically derived $w^2(l, t)$. Log-log plots of $w^2(l, t)$ against l at $t = 18$ (left panel) and of $w^2(l_{\max}, t)$ against t (right panel). The light-gray lines indicate the numerically obtained values with different sample paths, dots indicate the average of $w(l, t)$ for different paths, and the black line indicates analytically obtained values. (b) Numerically obtained parameter dependency of the Hurst exponent α on c and ρt. (c) The parameter dependency of the growth exponent β on ρct and ρt. Dots indicate the numerically obtained growth exponents, and the line indicates the plot of (15).

nents were determined by the index c and ρt, where

$$c = \frac{(v_l - v_f)^2 p_l (1 - p_l)}{\rho \sigma^2}. \tag{14}$$

The plots of the Hurst exponents against $\log c$ with different ρt are shown in Fig. 5(b). When the difference in cell motility $(v_l - v_f)$ is relatively large, c takes a large value and α approaches $\alpha = 0.91$, corresponding to the fixed-noise model. On the other hand, when the random component of the cell movement (σ) is relatively large, c is small and α approaches $\alpha = 0.48$, corresponding to the EW model.

The growth exponents β were also regarded as a two-variable function of ρt and c. From the theoretical consideration (see the Supplemental Material D [30]), we can calculate β as follows:

$$\beta = \frac{2(2 - \sqrt{2})\gamma + 1}{\frac{8}{3}(2 - \sqrt{2})\gamma + 4}, \tag{15}$$

where $\gamma = \rho ct$ and we assumed that N and ρt are sufficiently large. Plots of β against $\log \gamma$ are shown in Fig. 5(c). It was shown that the random cell movement decreases β. However, after sufficient time has passed, β always takes a value of 0.75, corresponding to the fixed-noise model.

E. Confirmation of analytical prediction

As described in this section, we experimentally examined the dependency of the Hurst and growth exponents derived from numerical and analytical considerations.

First, the effect of the initial size of the monolayer was examined. A monolayer of 3-mm diameter was prepared, and

its spreading was observed. The Hurst and growth exponents were $\alpha = 0.837$ and $\beta = 0.740$, respectively, confirming that the scaling property of the growing contour was independent of the number of cells (Fig. S5 [30]). Thus, this result was reproduced by the same parameters used in Fig. 2.

Next, we investigated how cell behavior affects the scaling property. Since it is known that cell behavior changes depending on the substrate [32,33], we prepared a collagen-coated culture dish and performed time-lapse observations of the MDCK cell monolayer from $t = 4$ to $t = 18$. The results of these observations are shown in Fig. 6(a) and Movie 5 in the Supplemental Material [30]. We found that the Hurst and growth exponents both decreased: $\alpha = 0.742$, $\beta = 0.687$. Meanwhile, the averaged expansion speed of $\langle D(\theta) \rangle$ was increased to 28.7 μm/h, which is 2.5 times higher than that of uncoated glass dish. In addition, we repeatedly measured the exponents in different monolayers and obtained that $\alpha = 0.749 \pm 0.012$ and $\beta = 0.687 \pm 0.050$, respectively. These values were not much different from the data shown in Fig. 6(a).

Using the results of the mathematical analysis [Figs. 5(b) and 5(c)], we estimated the parameters that would reproduce the experimental data in Fig. 6(a). We derived the value of $\gamma = \rho ct$ such that the growth exponent $\beta = 0.687$ was satisfied in (15), and we found $\gamma = 17.8$. Here, we assumed that while the difference of the substrate affects the motility of the cell, the effects on cell-cell adhesion and the proportion of leader cells are small. Thus, the values of ρ and p_l are regarded as identical to those in the control (Fig. 4): $\rho = 6.67$, $p_l = 0.1$. We obtained $c = 0.148$ and could then determine the values of σ^2 and $(v_l - v_f)^2 p_l (1 - p_l)$ to match the values of $w(l_{\max}, t)$. In addition, the time evolution of the mean diameter is 23.8 μm/h, which is equal to $v_l p_l + v_f (1 - p_l)$, so both v_l and v_f can be estimated. The values for the estimated parameters were $v_l = 123$, $v_f = 18.2$, and $\sigma = 31.8$.

At the same time, the parameters can also be estimated by the Hurst exponents using the relationship in Fig. 5(b). We estimated that $c = 0.19$ from $\rho t = 120$ and $\alpha = 0.749$. The parameter values are obtained in the same manner: $v_l = 126$, $v_f = 17.9$ and $\sigma = 28.8$. The estimated parameter sets from Hurst and growth exponents take close values. This result shows that the Hurst and growth exponents under the different conditions are also consistent with our model. Figures 6(b), S6 and Movie 6 in the Supplemental Material [30] show the results of numerical calculations using the parameters $v_l = 126$, $v_f = 17.9$, and $\sigma = 28.8$. These estimated parameters reproduced the experimental results.

Next, we confirmed the consistency between theoretically estimated and experimentally observed cell motility. The experimental results [shown in Fig. 6(a)] were reproduced in our model by assuming that the motility of the follower cell (v_f) and the intensity of random cell movement (σ) both increased about ninefold from the parameters used in Fig. 2. Figure 6(c) and Movie 7 in the Supplemental Material [30] show the cell motilities on the different cell culture substrates. The total path lengths of the single cell for 2 h were measured: 6.4 μm/h for the uncoated glass dish and 30.1 μm/h for the collagen-coated dish. The motility of the cells on the collagen increase 4.7-fold. This value is not exactly matched to the theoretical prediction; however, the order of the values is not
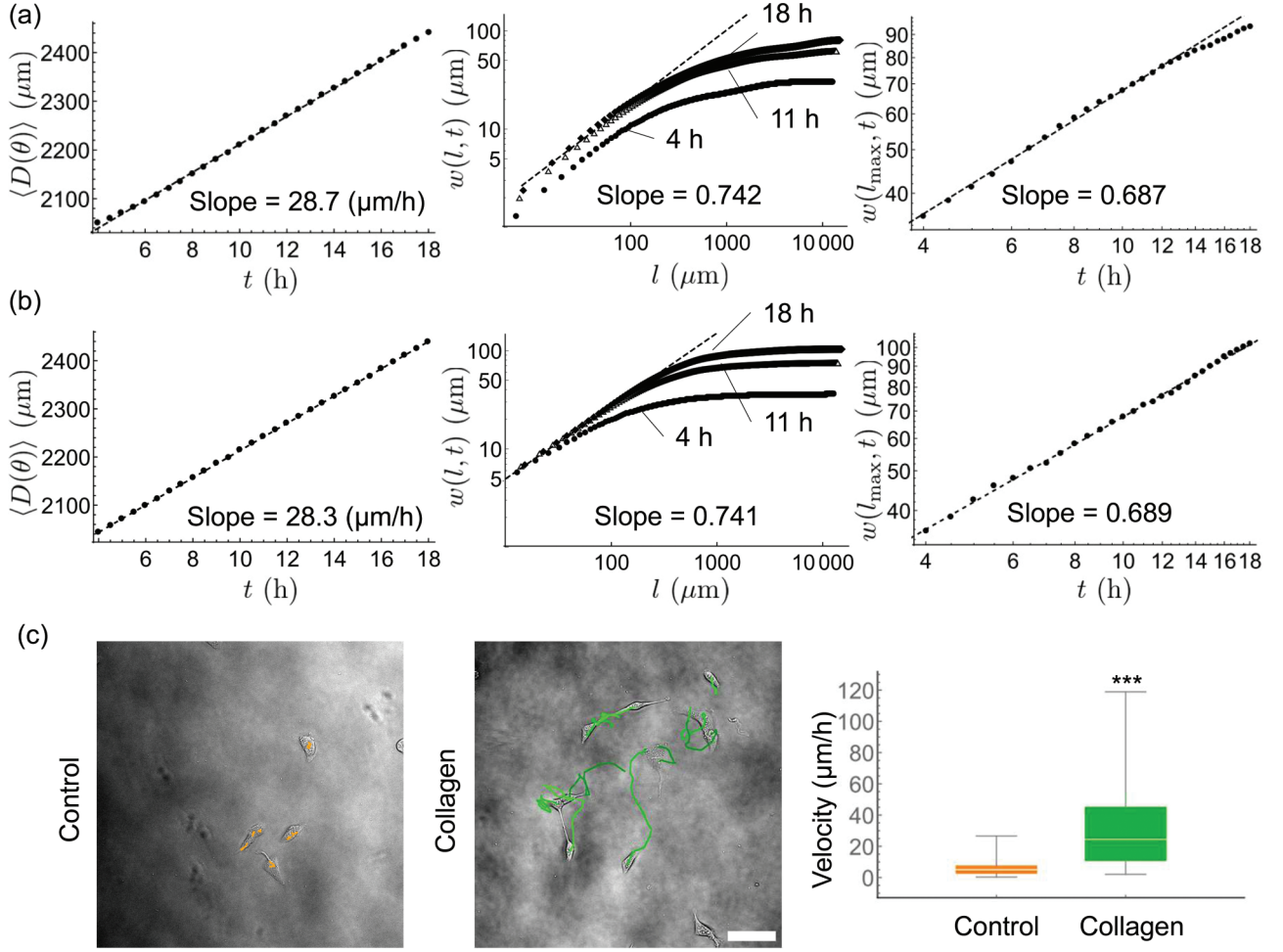
FIG. 6. The experimental result with 100 mg/L type I collagen-coated dish is also reproduced by the model (3). (a) Experimental results. Time evolution of averaged $D(\theta)$ (left panel), log-log plot of the local roughness $w(l, t)$ and l (middle panel), and log-log plot of $w(l_{\max}, t)$ and t (right panel). Dots indicate the experimentally obtained data and the dashed line is the fitted line for the data. (b) Numerical results corresponding to panels (a). Parameters: $v_l = 126$ [μm h^{-1}], $v_f = 17.87$ [μm h^{-1}], $p_l = 0.1$, $\rho = 6.67$ [h^{-1}], and $\sigma = 28.8$ [μm h$^{-1/2}$]. (c) Single-cell movement assay. The trajectories of the cell nuclei are indicated by the colored lines in the uncoated glass dish (left panel) and the collagen-coated dish (middle panel). Right panel shows the velocity of the cells; 6.36 μm/h in the uncoated glass dish and 30.1 μm/h in the collagen-coated dish. *** p-value $= 3.68 \times 10^{-9}$; scale bar $= 100$ μm.

far off. Therefore, the experimental results under the different conditions were consistent with the analytically predicted parameter dependency of the exponents, and the parameters to reproduce the experiment are quantitatively reasonable. These results further confirm that the contour formation of MDCK cells is generally well explained by our model.

IV. DISCUSSION

Our purpose is to clarify the mechanism underlying the dynamic scaling law for the contour of epithelial cell monolayer. In this study, we have proposed a framework that explains the macroscopic property of the contour from the microscopic cell behavior. We found that the time evolution of the contour satisfied the dynamic scaling law: $\alpha = 0.86$ and $\beta = 0.73$. From the observation results, we constructed a simple mathematical model and demonstrated that the contour shape arose from the behavior of the cells at the sheet edge. Our mathematical anal-

ysis of the model suggested that the presence of leader cells is essential for the observed pattern formation. We found that the Hurst and growth exponents were dependent on the ratio of the variance of cell motilities to the intensity of the random cell movement. The theoretical prediction was experimentally confirmed by changing the cell motilities.

The study of mathematical models of collective cell movement has attracted significant attention over the past decade, especially within the fields of statistical mechanics and biophysics [34]. The models can be categorized into continuous models and discrete models. In continuous models, the cell colony is regarded as a continuum. Such models have been constructed mainly to explain the fingering instability of the epithelial sheet [11,33,35–38]. On the other hand, in discrete models, each cell has been represented by polygons or particles. In the former case, the classical vertex model with chemotaxis and fluid properties [39] and the active vertex model [40], which also added the effect as an active fluid, have

been proposed. In the latter, a particle model mostly included the cell-cell interactions and the random kinetic components. The model explicitly introduced leader cells [41], and a model with the effects of the bending and the surface tension have been proposed [42]. Such models are preferable for explaining experimental data, and they allow an analytical understanding of the relationship between the physical quantity and the dynamics. In a sense, our model can be understood as the simplest form of the discrete particle model. To understand the scaling properties, a simpler model is preferable, because it is necessary to consider the relationship between power spectra for various wave numbers. The reason we used the spatially discrete model was to describe the differences of the motilities among the cells, such as leader or follower cells. The result that even the simple model explained the dynamic scaling within the contour shape suggested that the random cell movement, the deterministic differences in cell motility, and the effects of intercellular adhesion have critical implications on the contour of the epithelial monolayer.

The EW and KPZ models are widely known to satisfy the dynamic scaling law, and it has been reported that the contour shape of HeLa and Vero cell colonies follows KPZ universality [24]. However, the MDCK cells observed here did not follow this universality. Possible reasons for this difference are the emergence of leader cells. In this study, we found that the leader cells emerge in the early stage and persist during observation. The differential motility of leader and follower cells corresponds to the temporally fixed noise in the model. On the other hand, the EW and KPZ equations do not contain the corresponding noise term. The EW equation with temporally fixed noise has recently been considered by Cagnetta *et al.* [43]. They focused on pattern formation of a membrane in the biological context, and they obtained scaling properties of the power spectra that are consistent with our results (10).

$D(\theta)$ cannot precisely capture the contour structure when convoluted contours with overhangs are formed. We confirmed, however, that the effects of the overhangs on the scaling property were small. First, we measured the outermost edge of the cell sheet as $D'(\theta)$ from the outside of the monolayer [Fig. S7(a)] [30], and quantified the fraction of data points that were affected by overhangs. The number of affected points increases with time, and the fraction is 11% at $t = 18$ h [Fig. S7(b)] [30]. Next, we measured the Hurst and growth exponents for $D'(\theta)$. The average difference between $D(\theta)$ and $D'(\theta)$ for each slope is 1.16% for the Hurst exponents, and 4.40% for the growth exponents (an example of the results is shown in Fig. S7(c) [30]). Finally, the reliability of the $D(\theta)$ is examined by the consistency between the Hurst exponents α and the box-count fractal dimensions $\mathcal{D}$. The box-count method is a procedure that calculates the fractal dimension from the contour shape itself; theoretically, $\alpha + \mathcal{D} = 2$. We confirmed that $2.006 < \alpha + \mathcal{D} < 2.064$ for six independent assays. These results suggest that the effects of the overhangs on the scaling property are limited within our time window.

However, after a long period, the quantitative consistency between our model and the experimental results is lost because the effect of the increasing number of cells, the overhang structure, and merging of the sheet protrusion are not considered. The global roughness $w(l_{\max}, t)$ started to devi-

ate from the power law at $t = 15$ h and gradually increased beyond $t = 20$ h (Fig. S8(a) [30]). Therefore, it is vital to evaluate the reliability of the scaling law obtained herein and determine whether the length of time we used was appropriate. The log-log plot of $w(l, t)$ against l with $t = 21.5, 23$ h shows a similar curve to that at $t = 18$ h (Fig. S8(b) [30]). In addition, the fractal dimension calculated by the box-count method was $\mathcal{D} = 1.15$ for the contour at $t = 96$ h (Fig. S8(c) [30]). The relationship between the box-count fractal dimension $\mathcal{D}$ and Hurst exponent α suggests that the spatial scaling law $\alpha = 0.85$ also holds at $t = 96$ h. These results show that the spatial scaling law was largely formed by $t = 18$ h, and that it was maintained for a long period. From these findings on the scaling properties, there would be two expansion systems. First, the contour of the monolayer evolves while the dynamic scaling law is satisfied, and when it gets sufficiently rough (at $t = 15 - 20$ h in our experiment), it ruffles slowly and keeps its spatial scaling law owing to the effect of the overhang and finger collisions. Herein, we discuss and clarify the mechanism of generating the dynamic scaling laws, and the length of time we used appears to be reasonable for its purpose. To reproduce the contour structure after a long period, it is necessary to construct the model that can handle the effect of the overhang structure and finger collisions [11]. It is still a great challenge to analytically understand the relationship between these effects and the scaling properties.

In our model (4), there are five parameters (v_l, v_f, p_l, ρ, σ). The proportion p_l was estimated from the distribution of cells with large lamellipodia [Figs. 3(b) and 3(c)]. The motilities v_l and v_f of the leader and follower cells, respectively, were of the same scale as the experimentally measured spreading speed, and the intensity of the random movement σ is also expected to have a similar scale. We estimated the scale of the stiffness ρ from the height of the protrusion. If the protrusion of the contour originates from a single leader cell, its height can be estimated as follows:

$$h_0(t) = (v_l - v_f)t(I_0(2\rho t) + I_1(2\rho t))e^{-2\rho t}. \qquad (16)$$

Here, I_0 and I_1 are the Bessel functions of the first kind. For the contour of $t = 4$ h, we found 27 protrusions, and their sizes were 56.44 ± 18.69 μm. By substituting the other parameters at $t = 4$ h, ρ is estimated to lie in the range $1.87 \leqslant \rho \leqslant 7.53$; the values used in the numerical simulation ($\rho = 6.67$) are included in this range. These results suggest that the five parameter values we used are both consistent with the experimental data and reliable.

The growth exponents obtained from analysis of the mathematical model, $\beta = 0.74$, were almost identical to those obtained numerically and experimentally, while the Hurst exponent, $\alpha = 0.80$, was smaller than those obtained by numerical calculations $\alpha = 0.85$. The value of $w(l, t)$ is defined as the mean of the standard deviation in the closed range l; however, this value cannot be directly calculated from the power spectra. Therefore, to estimate the Hurst exponent, the expected value of the variance was calculated, and the square root of this value was taken to estimate the value of $w(l, t)$. The value of $\sqrt{w^2(l, t)}$ is not the same as $w(l, t)$, since the mean of the standard deviation in a given interval differ from the square root of the mean of the variance. On the other

hand, for the growth exponents, we calculate global roughness $w(l_{\max}, t)$ as the standard deviation with respect to the entire direction. Since this value is equal to the square root of the variance, it is close to the values obtained numerically.

The expected values of the power spectra (10) converge to the constant values when $\rho t \to \infty$. Since $w^2(l, t)$ is represented by the linear sum of the power spectra, $w^2(l, t)$ also converges to constant values. Therefore, it is suggested that α at $\rho t \to \infty$ is determined by c, and that there is a critical value c^* such that when $c \ll c^*$, the scaling law $\alpha = 0.5$, $\beta = 0.25$ was obtained, and when $c \gg c^*$, $\alpha = 0.9$, $\beta = 0.75$ was obtained. The value of c^* was estimated from the analytically obtained relationship between the expected values of $w^2(l, t_\infty)$.

The equation known as the quenched Edwards-Wilkinson (QEW) equation [17,44] is a model with the noise term dependent on x and h and the driving force $\mathcal{F}$ as follows:

$$\frac{\partial}{\partial t} h(x, t) = \rho \nabla^2 h(x, t) + \mathcal{F} + \eta(x, h(x, t)). \quad (17)$$

In this model, when $\mathcal{F}$ is sufficiently large and the noise term is considered to be spatially and temporally indepen-dent, then the system could be described as the EW equation: $\alpha = 0.5$, $\beta = 0.25$. However, the transition to a different dynamic scaling law $\alpha = 1.0$ and $\beta = 0.75$ occurs when $\mathcal{F} \ll \mathcal{F}_c$ [17,44,45]. The relationship between $\mathcal{F}_c$ and the scaling law is similar to the relationship between c^* and the scaling law in our model (7), which suggests that our models could be described as QEW-type models. However, we expect that more complex theoretical methods are required to solve this problem, and these remain a topic for future research.

The code used for this study is available from the corresponding authors upon request.

[1] R. A. Weinberg, *The Biology of Cancer*, 2nd ed. (Garland Science, New York, 2013).

[2] F. E. Lennon, G. C. Cianci, N. A. Cipriani, T. A. Hensing, H. J. Zhang, C. Chen, S. D. Murgu, E. E. Vokes, M. W. Vannier, and R. Salgia, Nat. Rev. Clin. Oncol. **12**, 664 (2015).

[3] O. Chepizhko, C. Giampietro, E. Mastrapasqua, M. Nourazar, M. Ascagni, M. Sugni, U. Fascio, L. Leggio, C. Malinverno, G. Scita, S. Santucci, M. J. Alava, S. Zapperi, and C. A. M. La Porta, Proc. Natl. Acad. Sci. USA **113**, 11408 (2016).

[4] R. Mayor and S. Etienne-Manneville, Nat. Rev. Mol. Cell. Bio. **17**, 97 (2016).

[5] A. J. Ridley, M. A. Schwartz, K. Burridge, R. A. Firtel, M. H. Ginsberg, G. Borisy, J. T. Parsons, and A. R. Horwitz, Science **302**, 1704 (2003).

[6] M. Poujade, E. Grasland-Mongrain, A. Hertzog, J. Jouanneau, P. Chavrier, B. Ladoux, A. Buguin, and P. Silberzan, Proc. Natl. Acad. Sci. USA **104**, 15988 (2007).

[7] M. Reffay, M. C. Parrini, O. Cochet-Escartin, B. Ladoux, A. Buguin, S. Coscoy, F. Amblard, J. Camonis, and P. Silberzan, Nat. Cell. Biol. **16**, 217 (2014).

[8] T. Omelchenko, J. M. Vasiliev, I. M. Gelfand, H. H. Feder, and E. M. Bonder, Proc. Natl. Acad. Sci. USA **100**, 10788 (2003).

[9] N. Yamaguchi, T. Mizutani, K. Kawabata, and H. Haga, Sci. Rep. **5**, 7656 (2015).

[10] J. Konen, E. Summerbell, B. Dwivedi, K. Galior, Y. Hou, L. Rusnak, A. Chen, J. Saltz, W. Zhou, L. H. Boise, P. Vertino, L. Cooper, K. Salaita, J. Kowalski, and A. I. Marcus, Nat. Commun. **8**, 15078 (2017).

[11] S. Mark, R. Shlomovitz, N. S. Gov, M. Poujade, E. Grasland-Mongrain, and P. Silberzan, Biophys. J. **98**, 361 (2010).

[12] H. G. Yevick, G. Duclos, I. Bonnet, and P. Silberzan, Proc. Natl. Acad. Sci. USA **112**, 5944 (2015).

[13] M. Vishwakarma, J. D. Russo, D. Probst, U. S. Schwarz, T. Das, and J. P. Spatz, Nat. Commun. **9**, 3469 (2018).

[14] R. Riahi, J. Sun, S. Wang, M. Long, D. D. Zhang, and P. K. Wong, Nat. Commun. **6**, 6556 (2015).

[15] R. F. Voss, Phys. D (Amsterdam, Neth.) **38**, 362 (1989).

[16] B. B. Mandelbrot, Phys. Scr. **32**, 257 (1985).

[17] P. Meakin, *Fractals, Scaling, and Growth Far from Equilibrium* (Cambridge University Press, Cambridge, UK, 2011).

[18] J. G. Moreira, J. K. L. da Silva, and S. O. Kamphorst, J. Phys. Math. Gen. **27**, 8079 (1994).

[19] F. Family and T. Vicsek, J. Phys. A. **18**, L75 (1984).

[20] J. Wakita, H. Itoh, T. Matsuyama, and M. Matsushita, J. Phys. Soc. Jpn. **66**, 67 (1997).

[21] S. N. Santalla, J. Rodríguez-Laguna, J. P. Abad, I. Marín, M. M. Espinosa, J. Muñoz-García, L. Vázquez, and R. Cuerno, Phys. Rev. E **98**, 012407 (2018).

[22] M. Myllys, J. Maunuksela, M. Alava, T. Ala-Nissila, J. Merikoski, and J. Timonen, Phys. Rev. E **64**, 036101 (2001).

[23] K. A. Takeuchi and M. Sano, J. Stat. Phys. **147**, 853 (2012).

[24] M. A. C. Huergo, M. A. Pasquale, P. H. González, A. E. Bolzán, and A. J. Arvia, Phys. Rev. E **85**, 011918 (2012).

[25] N. E. Muzzio, M. A. Pasquale, P. H. González, and A. J. Arvia, J. Biol. Phys. **40**, 285 (2014).

[26] S. F. Edwards and D. R. Wilkinson, Proc. R. Soc. London, Ser. A **381**, 17 (1982).

[27] M. Kardar, G. Parisi, and Y. C. Zhang, Phys. Rev. Lett. **56**, 889 (1986).

[28] D. Roy and R. Pandit, Phys. Rev. E **101**, 030103(R) (2020).

[29] K. A. Takeuchi, Phys. A (Amsterdam, Neth.) **504**, 77 (2018).

[30] See Supplemental Material at http://link.aps.org/supplemental/10.1103/PhysRevE.102.062408 for additional information, figures, and videos.

[31] J. Tinevez, N. Perry, J. Schindelin, G. M. Hoopes, G. D. Reynolds, E. Laplantine, S. Y. Bednarek, S. L. Shorte, and K. W. Eliceiri, Methods **115**, 80 (2017).

[32] H. Haga, C. Irahara, R. Kobayashi, T. Nakagaki, and K. Kawabata, Biophys. J. **88**, 2250 (2005).

[33] C. Pérez-González, R. Alert, C. Blanch-Mercader, M. Gómez-González, T. Kolodziej, E. Bazellieres, J. Casademunt, and X. Trepat, Nat. Phys. **15**, 79 (2019).

[34] V. Hakim and P. Silberzan, Rep. Prog. Phys. **80**, 076601 (2017).

[35] G. Y. Ouaknin and P. Z. Bar-Yoseph, Biophys. J. **97**, 1811 (2009).

[36] P. Lee and C. W. Wolgemuth, PLoS Comput. Biol. **7**, e1002007 (2011).

[37] M. H. Köpf and L. M. Pismen, Soft Matter **9**, 3727 (2013).

[38] R. Alert, C. Blanch-Mercader, and J. Casademunt, Phys. Rev. Lett. **122**, 088104 (2019).

[39] M. Salm and L. M. Pismen, Phys. Biol. **9**, 026009 (2012).

[40] D. L. Barton, S. Henkes, C. J. Weijer, and R. Sknepnek, PLoS Comput. Biol. **13**, e1005569 (2017).

[41] N. Sepúlveda, L. Petitjean, O. Cochet, E. Grasland-Mongrain, P. Silberzan, and V. Hakim, PLoS Comput. Biol. **9**, e1002944 (2013).

[42] V. Tarle, A. Ravasio, V. Hakim, and N. S. Gov, Integr. Biol. **7**, 1218 (2015).

[43] F. Cagnetta, M. R. Evans, and D. Marenduzzo, EPJ Web Conf. **230**, 00001 (2020).

[44] D. A. Kessler, H. Levine, and Y. Tu, Phys. Rev. A **43**, 4551 (1991).

[45] O. Narayan and D. S. Fisher, Phys. Rev. B **48**, 7030 (1993).